Available online at www.sciencedirect.com
ScienceDirect
International Journal of Heat and Mass Transfer 51 (2008) 844–852
International Journal of HEAT and MASS TRANSFER
www.elsevier.com/locate/ijhmt

Numerical simulation of liquid-encapsulant float zone growth of indium phosphide crystals in zero gravity

Mingwei Li [a,b,*], Chunmei Liu [c], Tingxia Zhu [a]

[a] Institute of Power Engineering, Chongqing University, Chongqing 400044, China
[b] Research Center of Biological Function Information and Instruments of Chongqing University by Second-Term National 985 Project, Chongqing University, Chongqing 400044, China
[c] Institute of Vehicle and Motive Power Engineering of Henan University of Science and Technology, Luoyang 471003, China

Received 26 December 2006; received in revised form 17 April 2007
Available online 27 July 2007

Abstract

Numerical simulation for flow, heat transfer and thermal stress for a 3 in. diameter liquid-encapsulated float zone growth of single-crystal InP is conducted by using the finite-element method under zero gravity condition. The results show that the crystal and feed rod rotation rate has a notable influence on the flow pattern in the melt. It also shows that the melt/crystal interface shape becomes more convex and the maximum value of thermal stress in the crystal reduces with increasing encapsulant thickness, decreasing pulling rate and decreasing the length of the melting zone.

Keywords: Float zone; Liquid encapsulant; InP; Fluid flow; Heat transfer; Thermal stress

1. Introduction

Indium phosphide (InP) is an important semiconductor material in the application of optoelectronic and high frequency devices. Compared with silicon, the growth of InP is much more difficult in terms of yield and quality control. One problem arising from the growth of InP (or GaAs) is the volatility of the grown material. In order to prevent the evaporation of the compounds liquid-encapsulated Czochraski (LEC) technique is used successfully and liquid-encapsulated float zone (LEFZ) technique is proposed [1]. As well known, the quality of the grown crystal is associated with the melt flow, heat transport in the whole furnace and the thermal stress in the crystal. Convective transport in the melt may lead to small-scale spatial oscillations of the crystal's dopant composition, which are called striations or microsegregation and/or large-scale variations of the crystal's dopant composition, which are caused by the macrosegregation. The main mechanisms include natural convection due to buoyancy, forced convection driven by crystal and (or) crucible (or feed rod) rotation and Marangoni convection due to surface tension gradient. Under zero gravity condition buoyance-driven convection does not exist, but the other two flow mechanisms must be considered. Furthermore, the dislocation generation in the crystal is closely associated with the thermal stress in the crystal, the latter depends on the temperature gradient in the crystal. So understanding the feature of the flow, heat transfer and the thermal stress is very significant for the practical engineering application.

There have been some works that have dealt with the modeling and simulation of growth systems of InP crystal with various levels of complexity. Linear stability analysis for the buoyancy convection during the LEC growth of compound semiconductor crystals with a steady, uniform, vertical magnetic field was performed, critical Rayleigh number was obtained for the weaker and stronger magnetic

* Corresponding author. Address: Institute of Power Engineering, Chongqing University, Chongqing 400044, China. Tel.: +86 023 65415008; fax: +86 023 65102473.
E-mail address: mwlizao@yahoo.com (M. Li).

0017-9310/$ - see front matter © 2007 Elsevier Ltd. All rights reserved.
doi:10.1016/j.ijheatmasstransfer.2007.04.049

Nomenclature

b_e	thickness of encapsulant
c_p	heat capacity
D_{max}	maximum deflection of the melt/crystal interface
$\mathbf{e}_\theta$	unit azimuthal vector
L	length of the melting zone
Ma	Marangoni number, $Ma = \gamma_T r_s t_m/\mu_l v_l$
$\mathbf{n}$	unit normal vector
p	pressure
Pe	Peclet number, $Pe = \rho_s c_{ps} V_s r_s/\lambda_l$
Pr_l	Prandtl number, $Pr_l = \mu_l c_{pl}/\lambda_l$
Pr_e	Prandtl number, $Pr_e = \mu_e c_{pe}/\lambda_e$
$q_{rad,i}$	net radiative heat flux per unit area on the surface
Q_s	total heat transfer across the melt/crystal interface
Re_f	Reynolds number, $Re_f = 2\pi r_s^2 \omega_f/v_l$
Re_s	Reynolds number, $Re_s = 2\pi r_s^2 \omega_s/v_l$
r_s	crystal radius
$\mathbf{t}$	unit tangential vector
T	temperature
$T_{a1}, T_{a2}, T_{a3}, T_{a4}, T_{a5}, T_{a6}$	ambient temperature
T_h	heater temperature
T_m	melting temperature
u	radial components of velocity
v	axial components of velocity
w	azimuthal components of velocity
$\mathbf{v}$	velocity vector
V_f	feed rod pulling rate
V_s	crystal pulling rate
ΔH_f	latent heat of fusion
ΔH_s	latent heat of solidification

Greek symbols

β	thermal volumetric expansion coefficient
ε	emissivity
γ_T	interface tension temperature coefficient between melt and encapsulant
λ	thermal conductivity
μ	dynamical viscosity
v	kinematic viscosity
ρ	density
σ_{max}	maximum value of Von Mises stress in the crystal
σ_{pint}	peak of Von Mises stress at the melt/crystal interface
$\boldsymbol{\tau}$	stress tensor
ω_f	angular rotation rate of feed rod
ω_s	angular rotation rate of crystal

Subscripts

e	B_2O_3 encapsulant
f	feed rod
i	index denoting melt or encapsulant
j	other material
l	melt
s	crystal
q	quartz sleeve

fields [2]. Morton et al. [3,4] treated the species transport in an InP melt during the magnetically stabilized LEC process. Dopant distributions in the crystal and in the melt at several different stages were present for several magnetic field strengths. The effect of the convective species transport on the segregation in both the melt and the crystal was emphasized. Zhang and his coworkers [5] simulated the high pressure, liquid-encapsulated Czochraski (HPLEC) growth of InP crystal, the effect of gas recirculation on melt flow and interface shape was studied. Their model incorporated flows induced by buoyancy and capillary forces and by crystal and crucible rotations, as well as the radiation heat loss from the melt and the crystal surface. Zou et al. [6] extended Zhang et al.'s work, calculated the thermal stress in the crystal and the redistribution of dopant in the melt. A 3D unsteady model including the interface shape calculation was presented in the entire LEC furnace for the first time [7]. A numerical simulation to study the batch operation of liquid-encapsulated vertical Bridgman (LEVB) crystal growth was conducted, the dynamic effects of some process parameters, including the ambient temperature distribution and the shape and anisotropic properties of the ampoule, on heat flow, the growth rate, and the interface shape were given [8]. Okano et al. [9] investigated the effect of crucible cap and crucible rotation on interface shape in vertical gradient freezing (VGF). A parallel adaptive finite element scheme was used to analyze the InP LEC melt flows, in their model only the melt phase was included [10]. From our knowledge, there is no research report for liquid-encapsulant float zone growth of InP up till now.

In the present paper, we extend our previous numerical investigation of LEC growth of InP [11] to a liquid-encapsulated float zone growth including the melt/crystal and melt/feed rod interface calculation. Conservation of energy and the Navier–Stokes equation are solved in both the melt and the liquid encapsulant with global heat transfer model including effects of convection and radiation. The thermal stress distribution in the crystal is calculated based on our solution for the temperature field. The effects of the thickness of encapsulant, crystal and feed rod rotation rate, the crystal pulling rate as well as the length of the melting zone on the flow, temperature field, the melt/crystal interface shape and thermal stress are discussed.

2. Model formulation

2.1. Physical model and basic assumptions

Schematic diagram adopted in the present analyses is shown in Fig. 1. Indium phosphide melt with 7.5 cm diameter and 4.5–6 cm height is encapsulated by boron oxide with thickness of b_e. The crystal and feed rod rotate in the opposite direction with ω_s and ω_f, respectively. The heater and ambient temperature of each segment are given. The width of the heater is 1 cm, and the widths of those segments for specified ambient temperature T_{a1}, T_{a2}, T_{a3}, T_{a4}, T_{a5} and T_{a6} are 6 cm, 8.25 cm, 2.5 cm, 2.5 cm, 8.25 cm and 6 cm, respectively. To simplify the problem, the following assumptions are introduced. (1) The system is in a pseudo-steady state and is axisymmetric. (2) The flow is laminar and both the InP melt and the boron oxide encapsulant are incompressible. (3) The melt/encapsulant interface is non-deformable. (4) No subcooling exists at the melt/crystal and melt/feed rod interfaces, i.e. the interface shapes coincide with the melting temperature isotherms. (5) Thermophysical properties of the melt are assumed to be constant except for the temperature dependencies of surface tension and the dynamic viscosity μ of boron oxide. (6) Crystal and the feed rod have the same thermophysical properties. (7) The crystal behaves as a thermoelastic solid. (8) Gravitational effects are negligible under zero gravity conditions.

2.2. Mathematical model

2.2.1. Governing equations

Under the above assumptions, the governing equations for flow and temperature field are given as follows.

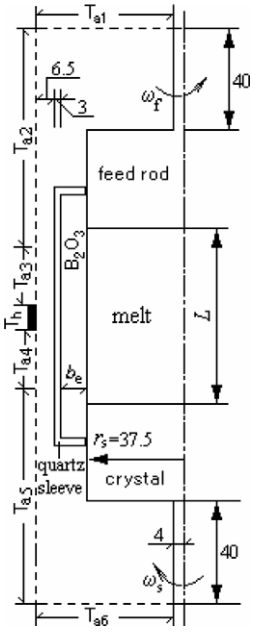

Fig. 1. Schematic diagram of a liquid-encapsulated floating zone growth of InP.

In the melt and encapsulant:

$$\nabla \cdot \mathbf{v}_i = 0, \tag{1}$$

$$\rho_i \mathbf{v}_i \cdot \nabla \mathbf{v}_i = -\nabla p_i - \nabla \cdot \boldsymbol{\tau}_i, \tag{2}$$

$$\rho_i c_{pi} \mathbf{v}_i \cdot \nabla T_i = \lambda_i \nabla \cdot \nabla T_i, \tag{3}$$

In the crystal:

$$\rho_s c_{ps} V_s \mathbf{e}_z \cdot \nabla T_s = \lambda_s \nabla \cdot (\nabla T_s). \tag{4}$$

In the feed rod:

$$\rho_f c_{pf} V_f \mathbf{e}_z \cdot \nabla T_f = \lambda_f \nabla \cdot (\nabla T_f). \tag{5}$$

In other solid materials:

$$\nabla \cdot (\nabla T_j) = 0. \tag{6}$$

where T, $\mathbf{v}$, p, and $\boldsymbol{\tau}$ are the temperature, velocity vector, pressure and stress tensor, respectively. Symbol ρ stands for the density, λ the thermal conductivity, c_p the specific heat, V_s the crystal pulling rate and V_f the feed rod pulling rate, respectively. Subscripts i, s, f and j indicate InP melt (i = l), B_2O_3 encapsulant (i = e), crystal, feed rod and other materials, respectively. Vector $\mathbf{e}_z$ is a unit vector parallel to z axis.

2.2.2. Boundary conditions for the temperature field

At the melt/encapsulant interface:

$$-\lambda_l \mathbf{n} \cdot \nabla T_l = -\lambda_e \mathbf{n} \cdot \nabla T_e + q_{rad,l}. \tag{7a}$$

At the melt/crystal interface:

$$\lambda_l \mathbf{n} \cdot \nabla T_l - \lambda_s \mathbf{n} \cdot \nabla T_s = \rho_s V_s \Delta H_s \mathbf{n} \cdot \mathbf{e}_z, \tag{7b}$$

$$T_l = T_s = T_m. \tag{7c}$$

At the melt/feed rod interface:

$$\lambda_l \mathbf{n} \cdot \nabla T_l - \lambda_f \mathbf{n} \cdot \nabla T_f = -\rho_f V_f \Delta H_f \mathbf{n} \cdot \mathbf{e}_z, \tag{7d}$$

$$T_l = T_f = T_m. \tag{7e}$$

At the encapsulated crystal sidewall:

$$-\lambda_s \mathbf{n} \cdot \nabla T_s = -\lambda_e \mathbf{n} \cdot \nabla T_e + q_{rad,s}. \tag{7f}$$

At the encapsulated feed rod sidewall:

$$-\lambda_f \mathbf{n} \cdot \nabla T_f = -\lambda_e \mathbf{n} \cdot \nabla T_e + q_{rad,f}. \tag{7g}$$

At the encapsulated quartz sleeve surface:

$$-\lambda_s \mathbf{n} \cdot \nabla T_s = -\lambda_e \mathbf{n} \cdot \nabla T_e + q_{rad,q}. \tag{7h}$$

At the exposed crystal sidewall and top:

$$-\lambda_s \mathbf{n} \cdot \nabla T_s = q_{rad,s}. \tag{7i}$$

At other exposed surfaces:

$$-\lambda_j \mathbf{n} \cdot \nabla T_j = q_{rad,j}. \tag{7j}$$

In these equations, $q_{rad,i}$ is the net radiative heat flux per unit area on the surfaces, and is given by

$$q_{rad,i} = \varepsilon_i \sigma_B \left[T_i^4 - \left(\sum_j A_j \varepsilon_j T_j^4 G_{ji} \right) / A_i / \varepsilon_i \right]. \tag{8}$$

where G_{ji} is Gebhart's absorption factor, which is the fraction of emission from surface A_j to A_i and absorbed, G_{ji} as well as the view factors between each surface element in the furnace are calculated using our code. ΔH_s, ΔH_f are the latent heat of solidification and fusion, respectively. Symbol **n** is the unit normal vector of the interface. ε the emissivity of melt, crystal, feed rod and quartz.

2.2.3. Boundary conditions for the flow field

At the melt/crystal and the encapsulant/crystal interface:

$$u_i = v_i = 0, \quad w_i = r\omega_s \ (i = 1 \text{ or } e). \tag{9a–c}$$

At the melt/feed rod and encapsulant/feed rod interface:

$$u_i = v_i = 0, \quad w_i = r\omega_f \ (i = 1 \text{ or } e). \tag{9d–f}$$

At the encapsulant/quartz sleeve surface:

$$u_e = v_e = w_e = 0. \tag{9g–i}$$

At the melt/encapsulant interface:

$$\mathbf{n}\cdot\mathbf{v}_l = 0, \mathbf{n}\cdot\mathbf{v}_e = 0, \tag{9j–k}$$

$$\boldsymbol{\tau}_l : \mathbf{nt} - \boldsymbol{\tau}_e : \mathbf{nt} = \gamma_T \nabla T_l \cdot \mathbf{e}_z, \tag{9l}$$

$$\mathbf{t}\cdot\mathbf{v}_l - \mathbf{t}\cdot\mathbf{v}_e = 0, \tag{9m}$$

$$\boldsymbol{\tau}_l : \mathbf{ne}_\theta - \boldsymbol{\tau}_e : \mathbf{ne}_\theta = \gamma_T \nabla T_l \cdot \mathbf{e}_\theta, \tag{9n}$$

$$\mathbf{e}_\theta\cdot\mathbf{v}_l - \mathbf{e}_\theta\cdot\mathbf{v}_e = 0. \tag{9o}$$

At the axis:

$$u_l = w_l = 0. \tag{9p, q}$$

where u, v, and w are the radial, axial and the azimuthal components of velocity, ω_s and ω_f are the angular rotation rates of the crystal and feed rod, respectively. Symbol γ_T denotes the temperature coefficient of interface tension between the melt and encapsulant, and **t** and $\mathbf{e}_\theta$ are the unit tangential and azimuthal vectors of each interface element, respectively.

We define the characteristic scales of the system by T_m and v_l/r_s for temperature and velocity, $(p - p_0 + \rho_l g z)$ for pressure, r_s for length, then the system is characterized by Reynolds number $Re_s = 2\pi r_s^2\omega_s/v_l$, $Re_f = 2\pi r_s^2\omega_f/v_l$, Marangoni number $Ma = \gamma_T r_s T_m/\mu_l v_l$, Peclet number $Pe = \rho_s c_{ps} V_s r_s/\lambda_l$, Prandtl number $Pr_l = \mu_l c_{pl}/\lambda_l$, and $Pr_e = \mu_e c_{pe}/\lambda_e$. Here μ is dynamical viscosity and v kinematic viscosity. These non-dimension numbers are listed in Table 1. By applying Galerkin finite-element method, the system gives a set of algebraic equations.

In the present work, the diameter of the crystal and the feed rod, the length of the melting zone, the heater and the ambient temperature are given. The crystal pull rate is determined as one of the unknown variables, together with velocities, pressures, temperatures and the interface coordinates, by simultaneously solving the set of nonlinear algebraic equations using Newton-Raphson method. The radiative heat exchange in the semi-transparent boric oxide layer is calculated by using the band-energy method [12]. The total number of elements, nodal points and unknowns are 16,014, 16,332 and 64,970, respectively. The number of elements only in melt is 10,106. The sizes of the minimum element in the melt are $\Delta r_{min} = 0.62$ mm, $\Delta z_{min} = 0.28$ mm. The number of elements in each direction is appropriate for the convergence of the solution. The error with increasing the number of elements in melt from 10,106 to 12,110 is less than 0.5%. Typical conditions are listed in Table 1, together with the thermophysical properties used in this work. Due to lack of the interface tension temperature coefficient of InP between the melt and encapsulant, the value of GaAs is applied to the present calculation. Numer-

Table 1
Physical properties and processing parameters

Melt		
Freezing temperature	T_m	1335 K
Density	ρ_l	5.05×10^3 kg/m^3
Dynamic viscosity	μ_l	8.19×10^{-4} kg/m s
Thermal conductivity	λ_l	2.2×10^1 W/m K
Specific heat	C_{pl}	4.24×10^2 J/kg K
Thermal volumetric expansion coefficient	β_l	4.44×10^{-4} 1/K
Emissivity	ε	0.3
Surface tension (between melt and B_2O_3) temperature coefficient	γ_l	-1.2×10^{-3} N/m K[12]
Prandtl number	Pr_l	0.0158
Latent heat of solidification	ΔH_s	7.35×10^2 kJ/kg
Crystal		
Density	ρ_s	4.73×10^3 kg/m^3
Thermal conductivity	λ_s	1.1×10^1 W/m K
Specific heat	C_{ps}	1.7×10^2 J/kg K
Emissivity	ε	0.6
Feed rod		
Density	ρ_f	4.73×10^3 kg/m^3
Thermal conductivity	λ_f	1.1×10^1 W/m K
Specific heat	C_{pf}	1.7×10^2 J/kg K
Emissivity	ε	0.6
Latent heat of fusion	ΔH_f	-7.35×10^2 kJ/kg
Boron oxide		
Density	ρ_e	1.648×10^3 kg/m^3
Dynamic viscosity	μ_e	$10^{-1.862+365/T}$ kg/m s
Thermal conductivity	λ_e	2.0 W/m K
Specific heat	C_{pe}	1.83×10^3 J/kg K
Thermal volumetric expansion coefficient	β_e	9.0×10^{-5} 1/K
Prandtl number	Pr_e	$9.15 \times 10^{0.138+3650/T}$
Quartz sleeve		
Thermal conductivity	λ_q	2.98 W/m K
Emissivity	ε	0.5
Other parameters		
Rotation rates of crystal	ω_s	2–4 rpm
Rotation rates of feed rod	ω_f	2–4 rpm
Marangoni number	Ma	4.52×10^8
Reynolds number	Re_s	$5.45 \times 10^4 \times \omega_s$
Reynolds number	Re_f	$5.45 \times 10^4 \times \omega_f$
Peclet number	Pe	0.0019–0.0076
Geometry		
Crystal radius	r_s	0.0375 m
Length of the melting zone	L	0.045–0.06 m
Encapsulant thickness	b_e	0.014–0.024 m

ical procedure used here is identical to our previous paper [13]. The thermal-elastic stress calculation is performed after the temperature distribution in the crystal has been obtained. The calculation of the thermal stress assumes that surface forces vanish on the surface of the crystal.

3. Results and discussion

A set of simulations under different operating conditions has been conducted. The effects of the thickness of encapsulant, the crystal and feed rod rotation rate, the crystal pulling rate and the length of the melting zone on the flow, heat transfer, melt/crystal interface shape and thermal stress are discussed in the following subsections.

3.1. Effect of encapsulant thickness

Fig. 2a–c and Table 2 present the effects of the thickness of encapsulant, b_e, on the flow, heat transfer, thermal stress and interface shape for a fixed crystal and feed rod rotation ($\omega_s = \omega_f = 3$ rpm) and a pulling rate ($V_s = 5$ mm/h) for a given length of the melting zone ($L = 5.25$ cm). Because the rotation rate of crystal and feed rod is identical, so in this case, the forced convective vortices in the melt driven by crystal and feed rod rotation, respectively, occupied their respective half zone. The thermocapillary convective cells are not easy to be seen, they are restricted to the very narrow region adjacent to the melt/encapsulant interface as indicated in the enlarged figure of the contours of stream

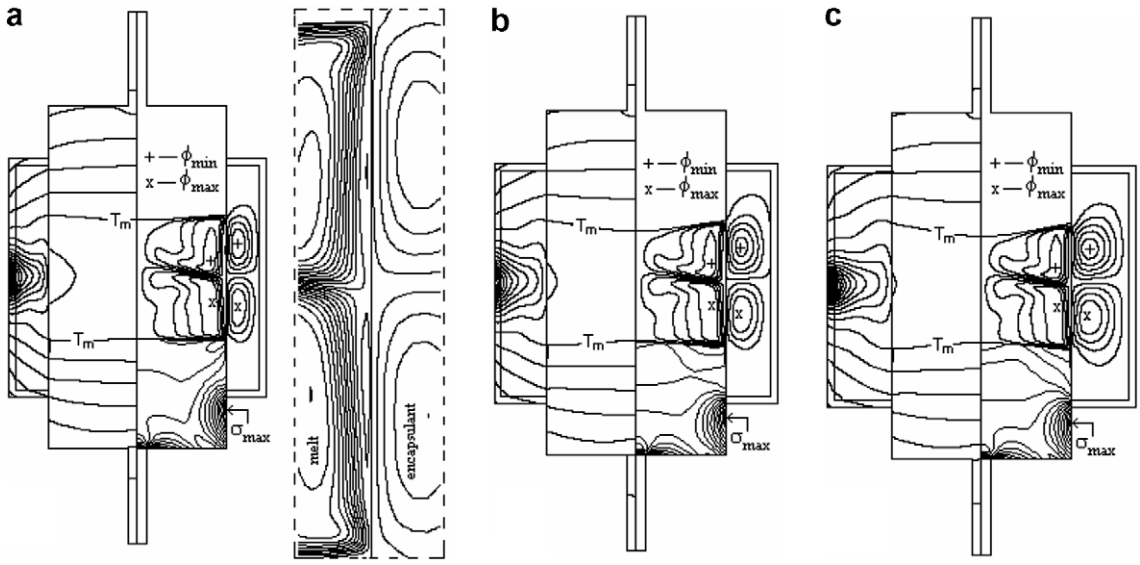

Fig. 2. Effect of encapsulant thickness. Isotherms separated by steps of 20 K (left), contours of stream function separated by 2×10^{-8} m^3/s (for melt and encapsulant) (right in the melt and encapsulant) and contours of Von Mises stress separated by 2 MPa (right in the crystal) under the conditions of $\omega_s = \omega_f = 3$ rpm, $V_s = 5$ mm/h and $L = 5.25$ cm. (a) $b_e = 1.4$ cm (an enlarged figure of the contours of stream function separated by 8×10^{-9} m^3/s for the melt near the melt/encapsulant interface attached at the right), (b) $b_e = 1.9$ cm, (c) $b_e = 2.4$ cm.

Table 2
Heater temperature and ambient temperature distribution and some representative parameters of the simulation results under different operating conditions

		T_h (K)	T_{a1} (K)	T_{a2} (K)	T_{a3} (K)	T_{a4} (K)	T_{a5} (K)	T_{a6} (K)	Q_s (W)	D_{maxs} (mm)	σ_{pint} (MPa)	σ_{max} (MPa)
$\omega_s = \omega_f = 3$ rpm, $V_s = 5$ mm/h, $L = 5.25$ cm	$b_e = 1.4$ cm	1986	1170	1239	1308	1289	1221	1153	118	0.2	5.45	31.3
	$b_e = 1.9$	1986	1177	1246	1315	1295	1227	1159	103	1.92	7.05	27.9
	$b_e = 2.4$	1998	1176	1245	1314	1296	1228	1160	96	2.74	9.01	24.4
$b_e = 1.4$ cm, $\omega_f = 3$ rpm,	$\omega_s = 2$ rpm	1987	1175	1244	1313	1286	1218	1151	119	0.96	6.61	31.6
$V_s = 5$ mm/h, $L = 5.25$ cm	$\omega_s = 4$ rpm	1986	1169	1238	1306	1294	1226	1157	113	−0.66	5.6	30
$b_e = 1.4$ cm, $\omega_s = 3$ rpm,	$\omega_f = 2$ rpm	1986	1170	1238	1307	1293	1225	1157	114	−0.4	5.13	30
$V_s = 5$ mm/h, $L = 5.25$ cm	$\omega_f = 4$ rpm	1986	1175	1246	1314	1286	1218	1151	120	−0.45	5.64	31.9
$b_e = 1.4$ cm, $\omega_s = \omega_f = 3$ rpm, $L = 5.25$ cm	$V_s = 2.5$ mm/h	1986	1165	1234	1302	1294	1226	1158	111	0.65	5.15	29.4
	$V_s = 7.5$ mm/h	1986	1176	1245	1314	1283	1215	1148	124	−0.64	6.53	33.1
	$V_s = 10$ mm/h	1986	1181	1251	1320	1277	1210	1143	130	−0.86	8.74	35
$b_e = 1.4$ cm, $\omega_s = \omega_f = 3$ rpm, $V_s = 5$ mm/h	$L = 4.5$ cm	1981	1165	1234	1303	1284	1216	1148	110	2.67	10	29.1
	$L = 6$ cm	2009	1175	1244	1313	1292	1224	1156	125	−1.39	11	34

function for the melt near the melt/encapsulant interface attached at the right in Fig. 2a. The flow in the encapsulant is characterized by two toroidal vortices, one is located in the upper half zone, whereas the other in the lower half zone. The convective flow in the encapsulant increase slightly when increasing the thickness of encapsulant from $b_e = 1.4$ cm to 2.4 cm which can be seen from the contours of stream function as shown in Fig. 2a–c. The improved convective heat transport in the encapsulant combining the larger area of the two sidewalls of the quartz sleeve, resulting in more heat being rejected to the surrounding from the quartz sleeve, so the heat transfer across the melt/crystal interface becomes less (from $Q_s = 118$ W to $Q_s = 96$ W when increasing the thickness of encapsulant from $h_e = 1.4$ cm to 2.4 cm as shown in Table 2) and a more convex (convex to melt) interface shape is observed in the situation of bigger thickness of $b_e = 2.4$ cm (see Fig. 3). This is in agreement qualitatively with numerical results of Thomas [14] and Croll [15]. The maximum Von Mises stress located at the outer surface of the crystal about 0.5 cm below the quartz sleeve. This is attributed to the high local temperature gradient due to the strong radiation heat exchange at this area. The maximum value of the Von Mises stress decreases from 31.3 MPa to 24.4 MPa when increasing the thickness of the encapsulant from 1.4 cm to 2.4 cm. Some of the these values are bigger than the typical maximum value of the Von Mises stress (25 MPa) for LEC-crystals as pointed out by Sahr et al. [16]. The high stress spots are more important to the generation of the dislocation. Meanwhile it should be emphasized that the critical resolved shear stress (CRSS) reduces rapidly with an increase of the temperature. The temperature at the melt/crystal interface is higher than anywhere else in the crystal, so the CRSS value will be lowest there. Therefore it is necessary to pay more attention to the value of thermal stress at the melt/crystal interface. In the present situation as indicated in Table 2, the peak value of the Von Mises stress at the melt/crystal interface increase from 5.45 MPa to 9.01 MPa when the thickness of the encapsulant increases from 1.4 cm to 2.4 cm.

From the analysis above, it is clear that not only the melt convection itself, but also the flow of the B_2O_3 encapsulant and the geometry configuration of the encapsulant have a significant impact on the heat transfer and the melt/crystal interface shape.

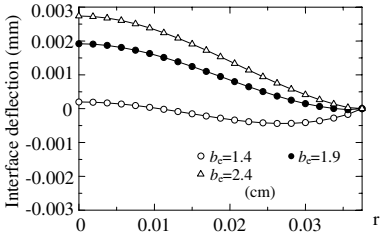

Fig. 3. Interface deflection under different thickness b_e ($\omega_s = \omega_f = 3$ rpm, $V_s = 5.0$ mm/h, $L = 5.25$ cm).

3.2. Effect of crystal and feed rod rotation

Crystal and feed rod rotation has a considerable effect on the flow pattern as shown in Fig. 4a–c. The flow pattern in the melt depends upon the crystal and feed rod rotation rate and their ratio. When the crystal and feed rod rotation rate is matchable, i.e. the absolute value of the ratio ω_s/ω_f is approximately equal to unity, as mentioned above, four-cell type flow in the melt appears as shown in Fig. 2a–c. In this case two forced convection cells and two thermocapillary convection cells co-exist, even though thermocapillary convection cells are very weak. When the absolute value of the ratio ω_s/ω_f is apart from unity the forced convection cells may penetrate the whole float-zone and merge one of the thermocapillary convection cell to form a combined bigger one (see Fig. 4a–c, a clearer enlarged figure of the contours of stream function for the melt near the melt/encapsulant interface is attached at the right of Fig. 4a). The remaining thermocapillary convection cell will never disappear, although it is restricted to the very narrow region adjacent to the melt/encapsulant interface.

By a detail comparison of the heater and ambient temperature listed in Table 2 and analysis of the flow and temperature field for the three different crystal rotation rates given by Fig. 4a–c, we can find that the heater and ambient temperature must be adjusted properly in order to maintain a fixed length and diameter of the melting zone. For example, for a given feed rod rotation rate ($\omega_f = 3$ rpm), with enhancing the crystal rotation rate from $\omega_s = 2$ rpm to 4 rpm, the ambient temperature at the crystal side should be increased slightly, i.e. T_{a4}, T_{a5} and T_{a6} increase from 1286 K to 1294 K, 1218 K to 1226 K and 1151 K to 1157 K, respectively, meanwhile the ambient temperature at the feed rod side should be decreased slightly, i.e.T_{a1}, T_{a2} and T_{a3} decrease from 1175 K to 1169 K, 1244 K to 1238 K and 1313 K to 1306 K, respectively, as shown in the Table 2. This is not difficult to understand when one considers the fact that more effective convective heat transport in the melt occurs at the higher rotation rate side, so corresponding ambient temperature should be improved properly. Comparing Fig. 4a and b, one can find that for the small crystal rotation rate of $\omega_s = 2$ rpm, the fluid heated by the melt/encapsulate interface can be more easily carried to the periphery above the melt/crystal interface by the combined cell, the center region above the melt/crystal interface (for a half section the dimensionless radius r is approximately in the range of 0–0.4) almost not be influenced by the melt convection, therefore the temperature gradient in the edge is larger in order to take away more heat to the surrounding as shown in Fig. 5, where the variation of the temperature gradient along the melt/crystal interface is plotted. On the contrary, for the higher crystal rotation rate ($\omega_s = 4$ rpm, see Fig. 4b), the crystal rotation driving flow cell combined with the upper thermocapillary convection cell enhances the convective heat transfer in the center region but decrease the heat transfer above the melt/crystal interface near the periphery. The total heat transfer

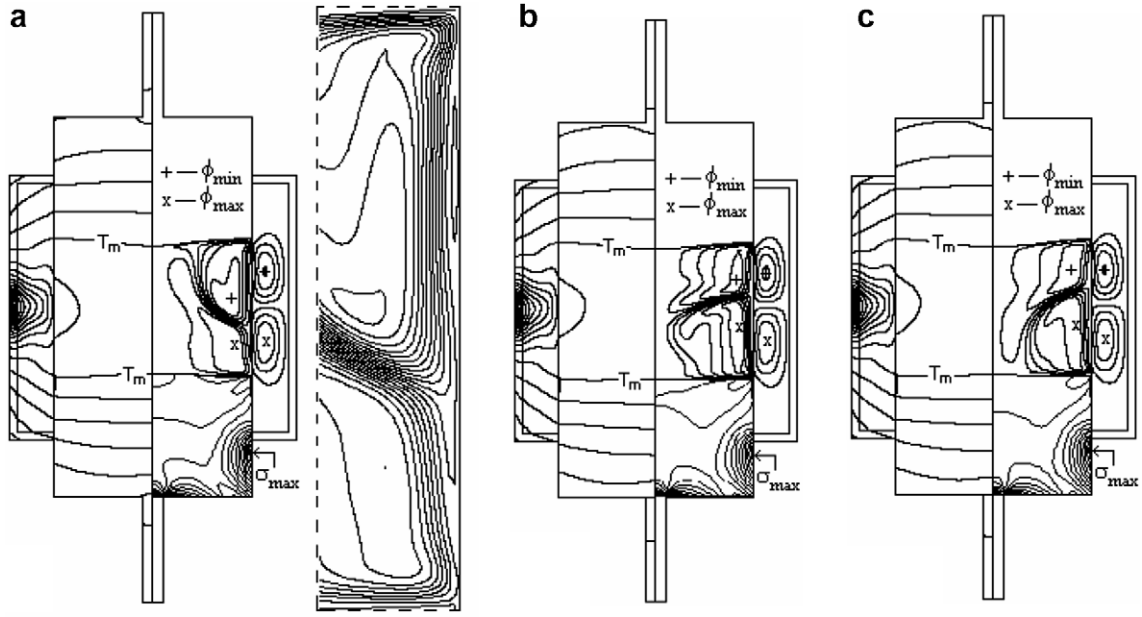

Fig. 4. Effect of crystal and feed rod rotation rate. Isotherms separated by steps of 20 K (left), contours of stream function separated by 2×10^{-8} m^3/s (for melt and encapsulant) (right in the melt and encapsulant) and contours of Von Mises stress separated by 2 MPa (right in the crystal) under the conditions of $b_e = 1.4$ cm, $V_s = 5$ mm/h, $L = 5.25$ cm. (a) $\omega_s = 2$ rpm, $\omega_f = 3$ rpm, (an enlarged figure of the contours of stream function separated by 8×10^{-9} m^3/s for the melt near the melt/encapsulant interface attached at the right), (b) $\omega_s = 4$ rpm, $\omega_f = 3$ rpm (c) $\omega_s = 3$ rpm, $\omega_f = 2$ rpm.

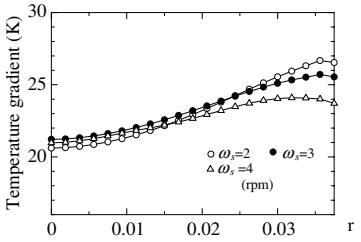

Fig. 5. Temperature gradient at the melt/crystal interface under different crystal rotation rate ω_s ($b_e = 1.4$ cm, $\omega_f = 3$ rpm, $V_s = 5.0$ mm/h, $L = 5.25$ cm).

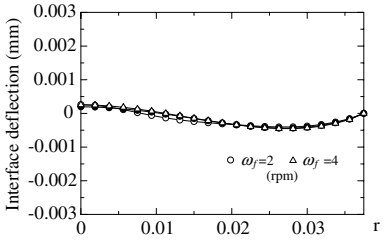

Fig. 7. Interface deflection under different feed rod rotation rate ω_f ($b_e = 1.4$ mm/h, $\omega_s = 3$ rpm, $V_s = 5.0$ mm/h, $L = 5.25$ cm).

across the melt/crystal interface Q_s reduces from 119 W to 113 K and the melt/crystal interface shape change from convex to concave (concave to the crystal) with increasing the crystal rotation rate from 2 to 4 rpm for a fixed feed rod rotation rate $\omega_f = 3$ rpm as shown in Fig. 6. The influence of the feed rod rotation on melt/crystal interface shape is negligible (see Fig. 7). The thermal stress does not change so much with the change of the crystal and feed rod rotation rate (see Table 2).

3.3. Effect of crystal pulling rate

Due to the space limitation, here we do not represent the isotherms and contours of stream function and Von Mises stress for various crystal pulling rate, but give some representative values as listed in Table 2 and the melt/crystal interface shapes as shown in Fig. 8. As a higher pulling rate is associated with a more release and absorb of the latent

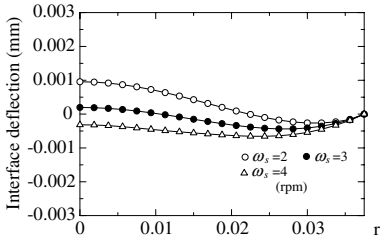

Fig. 6. Interface deflection under different crystal rotation ω_s ($b_e = 1.4$ mm/h, $\omega_f = 3$ rpm, $V_s = 5.0$ mm/h, $L = 5.25$ cm).

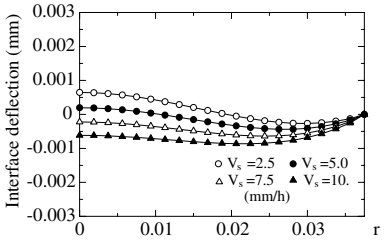

Fig. 8. Interface deflection under different pulling rate V_s ($b_e = 1.4$ mm/h, $\omega_s = \omega_f = 3$ rpm, $L = 5.25$ cm).

heat at the melt/crystal and melt/feed rod interface, respectively, so with the increase of pulling rate, the ambient temperature at the crystal side (T_{a4}, T_{a5} and T_{a6}) should be cut down and the ambient temperature at the feed rod side (T_{a1}, T_{a2} and T_{a3}) should be raised up reasonably as given in Table 2. Meanwhile, it should be emphasized that the solidification heat generated at the melt/crystal interface must be carried away mainly by the crystal, as pointed out by Lan [8] that higher axial thermal gradients could remove the heat of fusion away more effectively, so in the present situation, the melt/crystal interface shape convents from convex to concave with increasing the pulling rate (see Fig. 8). The maximum deflection of the melt/crystal interface reaches to −0.86 mm in the case of $V_s = 10$ mm/h. There exist no noticeable difference in the melt flow pattern with enhancing the pulling rate. The maximum Von Mises stress appearing at the sidewall of the crystal and the peak stress at the melt/crystal interface increase by 69.7% and 19%, respectively, as improving the pulling rate from 2.5 mm/h to 10 mm/h.

3.4. Effect of the length of the melting zone

The effect of the length of the melting zone, L, on the flow, heat transfer, thermal stress and the melt/crystal interface shape is shown in Fig. 9a,b. and Fig. 10. The shapes of the flow cells in the melt change with the change of the length of the melting zone. The highlight feature is the change of the melt/crystal interface shape from convex to concave (to the crystal) when increasing the length of the

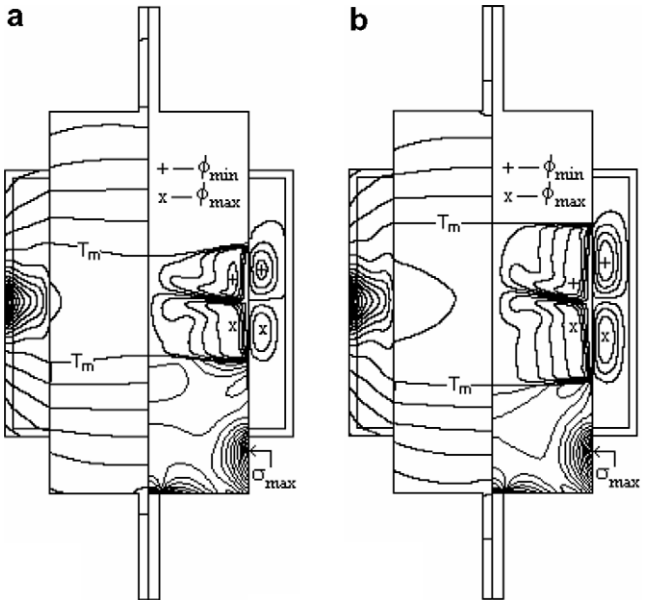

Fig. 9. Effect of the length of melting zone. Isotherms separated by steps of 20 K (left), contours of stream function separated by 2×10^{-8} m^3/s (for melt and encapsulant) (right in the melt and encapsulant) and contours of Von Mises stress separated by 2 MPa (right in the crystal) under the conditions of $b_e = 1.4$ cm, $\omega_s = \omega_f = 3$ rpm, $V_s = 5$ mm/h. (a) $L = 4.5$ cm, (b) $L = 6$ cm.

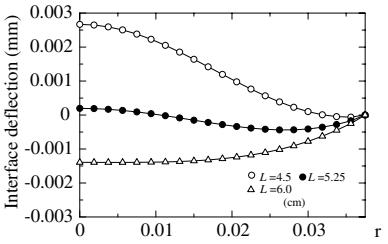

Fig. 10. Interface deflection under different length of the melting zone L ($b_e = 1.4$ mm/h, $\omega_s = \omega_f = 3$ rpm, $V_s = 5.0$ mm/h).

melting zone. The maximum deflection of the melt/crystal interface reaches to 2.67 mm as $L = 4.5$ cm. The heater and the ambient temperature needed for the long melting zone is larger than that of short melting zone as indicated in Table 2.

From the four values, Q_s, D_{maxs}, σ_{pint} and σ_{max} given in Table 2, one can find that the Von Mises stress at the melt/crystal interface is sensitive to the melt/crystal interface shape and deflection. Generally speaking, flatter melt/crystal interface corresponds to lower value of thermal stress at the melt/crystal interface, for example, the peak value of the Von Mises stress at the melt/crystal interface is 5.45 MPa (the lowest one) when maximum deflection of the melt/crystal interface is 0.2 mm (the flattest interface case) in the case of $b_e = 1.4$ cm, $\omega_s = \omega_f = 3$ rpm, $V_s = 5$ mm/h and $L = 5.25$ cm. Meanwhile concave interface will lead to a higher thermal stress than that of convex interface for the same magnitude of deflection, for example, the peak value of the Von Mises is 5.15 MPa for the convex interface of $D_{max} = 0.65$ mm in the case of $V_s = 2.5$ mm/h, $b_e = 1.4$ cm, $\omega_s = \omega_f = 3$ rpm and $L = 5.25$ cm and the extreme value of the Von Mises is 6.53 MPa for the concave interface of $D_{max} = -0.64$ mm in the case of $b_e = 1.4$ cm, $V_s = 7.5$ mm/h, $\omega_s = \omega_f = 3$ rpm and $L = 5.25$ cm. This is consistent with the results of reference [5]. As a whole, the deflection of the melt/crystal interface in the case of growth of the InP crystal is less than that one of GaAs crystal growth. This conclusion can be found by comparing the present results with these of reference [1]. On the other hand, from the data listed in Table 2 it is noted that the maximum value of the thermal stress of the crystal is related to the heat transfer crossing the melt/crystal interface, the maximum value of the thermal stress is proportional to the total heat transfer from the melt/crystal interface.

4. Concluding remarks

Taking the melt/crystal and melt/feed rod interface shape into account, the characteristics of flow and heat transfer as well as the thermal stress in LEFZ growth of InP are studied numerically for the first time by using a float zone simulation code. The results indicate that: (1) The encapsulant thickness changes the conditions of the radiation on the two sidewalls of the quartz sleeve and con-

vective heat transport in the encapsulant, this results in a change of the interface shape and the thermal stress. When increase the thickness of the encapsulant, the melt/crystal interface shape will become more convex, the maximum value of the Von Mises stress in the crystal located on the sidewall decreases, however the peak of the thermal stress at the melt/crystal interface increases. (2) The crystal and feed rod rotation rate has a remarkable effect on the flow pattern. The flow pattern in the melt depends on the crystal and feed rod rotation rate, in particularly, on their ratio. The heater and ambient temperature needed to be adjusted properly for suiting for a specific crystal and feed rod rotation rate. The melt/crystal interface shape will be influenced by the crystal rotation rate to some extend, but not by feed rod rotation rate. The Von Mises stress does not changes so much with the change of the crystal and feed rod rotation rate. (3) The effect of the length of the melting zone upon the melt/crystal interface shape is significant. Furthermore we note that the effect of the pulling rate on the melt/crystal interface deflection for InP floating zone growth is not negligible. The maximum value of thermal stress in the crystal decreased with reducing the pulling rate or shortening the length of the melting zone.

In principle, the melt/encapsulant interface is not flat and non-deformable even though under zero gravity circumstance, the assumption of non-deformable should be released in the further simulation.

Acknowledgements

This work was supported by NSFC (50676113, 50376078) and by NCET (05-0761).

References

[1] M.W. Li, W.R. Hu, S.X. Chen, Numerical investigation of FZ-growth of GaAs with encapsulant, Int. J. Heat Mass Transfer 47 (2004) 2941–2947.

[2] J.S. Walker, D. Henry, H. BenHadid, Magnetic stabilization of the buoyant convection in the liquid encapsulated Czochralski process, J. Cryst. Growth 243 (2002) 108–116.

[3] J.L. Morton, N. Ma, D.F. Bliss, George G. Bryant, Dopant segregation during liquid encapsulated Czochralski crystal growth in a steady axial magnetic field, J. Cryst. Growth 242 (2002) 471–485.

[4] J.L. Morton, N. Ma, D.F. Bliss, George G. Bryant, Magnetic field effects during liquid encapsulated Czochralski growth of doped photonic semiconductor crystals, J. Cryst. Growth 250 (2003) 174–182.

[5] H. Zhang, V. Prasad, D.F. Bliss, Modeling of high pressure, liquid-encapsulated Czochraski growth of InP crystal, J. Cryst. Growth 169 (1996) 250–260.

[6] Y.F. Zou, G.-X. Wang, H. Zhang, V. Prasad, D.F. Bliss, Macro-segregation, dynamics of interface and stresses in high pressure LEC grown crystal, J. Cryst. Growth 180 (1997) 524–533.

[7] E.N. Bystrova, V.V. Kalaev, O.V. Smirnova, E.V. Yakovlev, Yu.N. Makarov, Prediction of the melt/crystal interface shape geometry in liquid encapsulated Czochralski growth of InP bulk crystals, J. Cryst. Growth 250 (2003) 189–194.

[8] C.W. Lan, C.C. Ting, Numerical investigation on the batch characteristics of liquid encapsulated vertical Bridgman crystal growth, J. Cryst. Growth 149 (1995) 175–186.

[9] Y. Okano, H. Kondo, S. Dost, Numerical study of interface shape control in the VGF growth of compound semiconductor crystal, J. Cryst. Growth 237–239 (2002) 1769–1772.

[10] D. Givoli, J.E. Flaherty, M.S. Shephard, Analysis of InP LEC melt flows using a parallel adaptive finite element scheme, J. Cryst. Growth 180 (1997) 510–516.

[11] M.W. Li, Ch. M. Liu, P.Q. Wang, Numerical simulation of LEC growth of InP crystal with an axial magnetic field, Int. J. Heat Mass Transfer 49 (2006) 1738–1746.

[12] F. Dupret, P. Nicodeme, Y. Ryckmans, P. Wouters, M.J. Crochet, Global modeling of heat transfer in crystal growth furnaces, Int. J. Heat Mass Transfer 33 (9) (1990) 1849–1871.

[13] M.W. Li, Y.R. Li, N. Imaishi, T. Tsukada, Global simulation of a silicon Czochralski furnace, J. Cryst. Growth 234 (2002) 32–46.

[14] P.D. Thomas, J.J. Derby, L.J. Atherton, R.A. Brown, Dynamics of liquid-encapsulanted Czochralski growth of gallium arsenide: comparing model with experiment, J. Cryst. Growth 96 (1989) 135–152.

[15] A. Croll, M. Schweizer, A. Tegetmeier, K.W. Benz, Floating-zone growth of GaAs, J. Cryst. Growth 166 (1996) 239–244.

[16] U. Sahr, G. Müller, Growth of InP substrate crystals by the vertical gradient freeze technique, in: Conf. Proc., 12th Semiconducting and Insulating Materials Conference, 2002, pp. 13–18.